cmgh
CELLULAR AND MOLECULAR GASTROENTEROLOGY AND HEPATOLOGY

ORIGINAL RESEARCH

PFKFB3-mediated Pro-glycolytic Shift in Hepatocellular Carcinoma Proliferation

Qianhui Dou,[1] Aaron K. Grant,[1] Cody Callahan,[1] Patricia Coutinho de Souza,[1] David Mwin,[1] Adam L. Booth,[2] Imad Nasser,[2] Marwan Moussa,[1] Muneeb Ahmed,[1] and Leo L. Tsai[1]

[1]Department of Radiology, Beth Israel Deaconess Medical Center, Harvard Medical School, Boston, Massachusetts; and
[2]Department of Pathology, Beth Israel Deaconess Medical Center, Harvard Medical School, Boston, Massachusetts

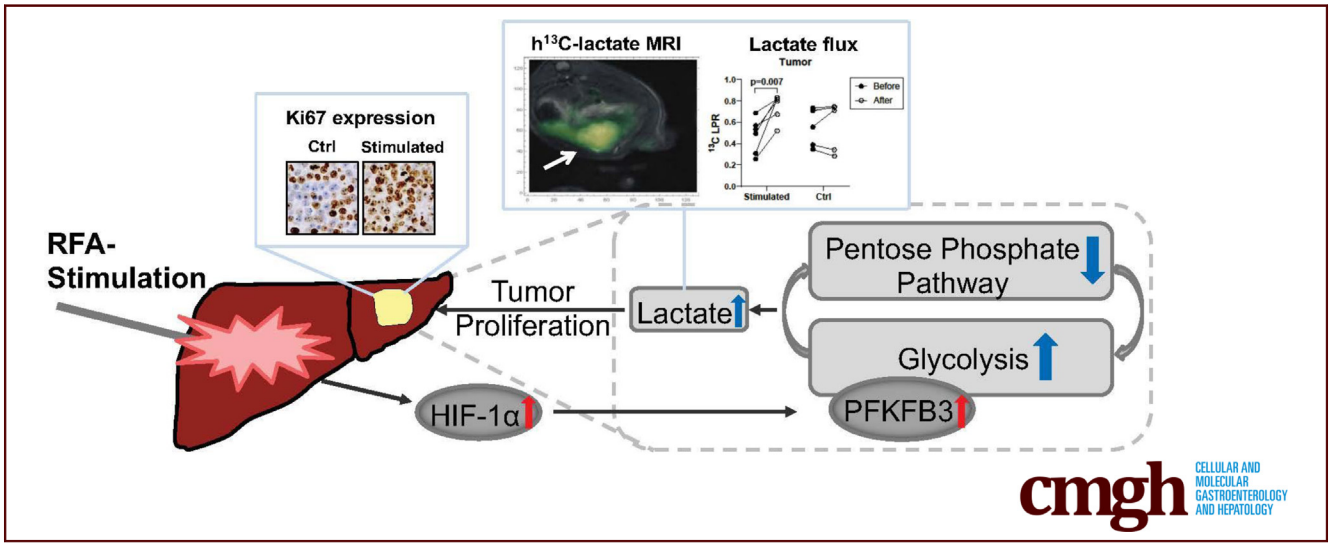

SUMMARY

The metabolic regulator PFKFB3 closely modulates lactate flux in hepatocellular carcinoma (HCC). Targeted inhibition was effective in preventing a switch to high-grade HCC, a process trackable with in vivo $h^{13}C$ magnetic resonance imaging. This offers a potential new theragnostic strategy for HCC.

BACKGROUND & AIMS: Metabolic reprogramming, in particular, glycolytic regulation, supports abnormal survival and growth of hepatocellular carcinoma (HCC) and could serve as a therapeutic target. In this study, we sought to identify glycolytic regulators in HCC that could be inhibited to prevent tumor progression and could also be monitored in vivo, with the goal of providing a theragnostic alternative to existing therapies.

METHODS: An orthotopic HCC rat model was used. Tumors were stimulated into a high-proliferation state by use of off-target liver ablation and were compared with lower-proliferating controls. We measured in vivo metabolic alteration in tumors before and after stimulation, and between stimulated tumors and control tumors using hyperpolarized ^{13}C magnetic resonance imaging (MRI) ($h^{13}C$ MRI). We compared metabolic alterations detected by $h^{13}C$ MRI to metabolite levels from ex vivo mass spectrometry, mRNA levels of key glycolytic regulators, and histopathology.

RESULTS: Glycolytic lactate flux increased within HCC tumors 3 days after tumor stimulation, correlating positively with tumor proliferation as measured with Ki67. This was associated with a shift towards aerobic glycolysis and downregulation of the pentose phosphate pathway detected by mass spectrometry. MRI-measured lactate flux was most closely coupled with PFKFB3 expression and was suppressed with direct inhibition using PFK15.

CONCLUSIONS: Inhibition of PFKFB3 prevents glycolytic-mediated HCC proliferation, trackable by in vivo $h^{13}C$ MRI. *(Cell Mol Gastroenterol Hepatol 2023;15:61–75; https://doi.org/10.1016/j.jcmgh.2022.09.009)*

Keywords: Aerobic Glycolysis; Hyperpolarized ^{13}C MRI.

Liver cancer is the fifth most common cancer worldwide and the third leading cause of cancer-related death. Hepatocellular carcinoma (HCC) represents more than 90% of primary liver cancer cases, and is often diagnosed at an advanced stage and refractory to existing systemic therapies.[1,2] Recent studies have shown that metabolic alterations are required in HCC progression.[3-5]

This is attributed to the necessity of cancers to maintain viability and build new biomass in a nutrient-poor environment.[6] Amino acids for protein synthesis, nucleic acid for DNA duplication, and lipids for cell biomembrane synthesis are all significantly altered to serve HCC proliferation and metastasis.[5,7] Metabolic pathways may offer targets for HCC tracking or therapy, but it remains unclear what the best diagnostic or treatment approaches are.

The tendency of cancer cells to favor aerobic glycolysis, known as the Warburg effect, is relatively inefficient but provides energy rapidly, resulting in high lactate production.[8-10] Pyruvate is located at an intersection of key pathways of metabolism. Intracellular pyruvate can be converted to acetyl Co-A to enter tricarboxylic acid cycle, lactate (in part due to the Warburg effect), or alanine via transamination. Hyperpolarized ^{13}C magnetic resonance imaging (h^{13}C MRI) enables in vivo real-time high-resolution imaging of the uptake and metabolism of ^{13}C-labeled tracer molecules including pyruvate.[11] Altered glycolysis was shown in McA-RH7777 hepatomas using in vivo h^{13}C MRI.[12] Latent HCC, in response to chemoembolization, has also demonstrated increased glycolytic dependency and lactate flux relative to alanine, supporting the notion that glycolysis plays a crucial role in HCC treatment response.[13]

The purpose of our study was to identify targetable factors in the glycolytic modulation of HCC that could also be tracked and monitored in vivo with h^{13}C MRI, a metabolic imaging modality which is clinically available.[11,14,15] To achieve this we used an orthotopic HCC model and exploited a phenomenon whereby tumor proliferation and aggression is stimulated by use of off-target hepatic radiofrequency ablation (RFA).[16-18] This effect has been linked to hypoxia-inducible factor 1-alpha (HIF-1α), which is known to transactivate several genes encoding glucose transporters and glycolysis including 6-phosphofructo-2-kinase/fructose-2,6-bisphosphatase-3 (PFKFB3), hexokinase 2 (HK2), glucose transporter 1 (GLUT1), lactate dehydrogenase A (LDHA), and monocarboxylate transporter 4 (MCT4).[19-23] This allows a controlled model using the same cell line and baseline tumors to generate high-grade and low-grade disease states.

We observed that N1S1 tumors with greater proliferation exhibited greater higher lactate flux as measured by h^{13}C MRI. We then identified the glycolytic regulator PFKFB3 as having the greatest correlation with lactate flux and proliferation. Lastly, we show suppression of N1S1 proliferation and lactate flux with targeted PFKFB3 inhibition. Our results show that glycolytic activity and suppression with PFKFB3 targeting are both trackable in vivo with h^{13}C MRI.

Results

Off-target Ablation Stimulates N1S1 Proliferation

Off-target hepatic RFA has been previously linked to increased growth of untreated and distal tumors,[24] and recurrent HCC in patients following RFA demonstrate higher grade disease associated with lower overall survival.[25] We found that the tumor volume change following RFA stimulation was significantly greater than in a control group (stimulation 1.7 ± 0.42 vs control 0.89 ± 0.21; $P = .029$; n = 4) (Figure 1). This is concordant with studies on other tumor models.[26]

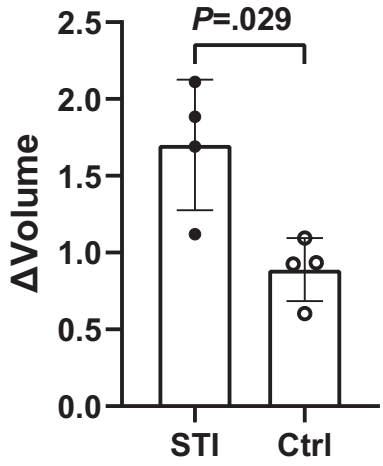

Figure 1. RFA of the liver promotes off-target HCC tumor growth. The volume change between baseline and 7 days post-stimulation/control (ΔVolume = $Volume_{after}$ − $Volume_{before}$) in both stimulated (STI) and control/sham (Ctrl) group. The comparison was performed with a Mann-Whitney test.

Increased Glycolysis in Stimulated N1S1 HCC is Detectable in Vivo by h^{13}C MRI and Correlates With Greater Tumor Proliferation

To understand the early changes of metabolism in tumor following stimulation, we measured metabolic alteration in rat liver in vivo at baseline and 3 days following off-target RFA (stimulated, high-grade HCCs) or a sham RFA (control, low-grade HCC) with h^{13}C MRI. Example images of ^{13}C-pyruvate and ^{13}C-lactate signal within tumors are shown in Figure 2, *A*. h^{13}C MRI was successful in all 12 rats/tumors at both baseline (before RFA or sham) and post-stimulation (after RFA or sham) timepoints with the exception of a single control rat post sham, where the spectroscopic data was only partially captured and could not be reliably compared with the other data; this MRI data point was therefore excluded from analyses. In tumors, the maximum signal of ^{13}C-pyruvate was approximately 6 seconds after injection,

Abbreviations used in this paper: **ANOVA, analysis of variance; APR, alanine to pyruvate ratio; BPR, bicarbonate to pyruvate ratio; GLUT1, glucose transporter 1; GPT1, alanine aminotransferase 1; h^{13}C MRI, hyperpolarized 13C magnetic resonance imaging; HCC, hepatocellular carcinoma; HIF-1a, hypoxia-inducible factor 1-alpha; HK2, hexokinase 2; LDHA, lactate dehydrogenase A; LPR, lactate to pyruvate ratio; MCT4, monocarboxylate transporter 4; mRNA, messenger RNA; PFKFB3, 6-phosphofructo-2-kinase/fructose-2,6-bisphosphatase-3; PKM, pyruvate kinase M; PPP, pentose phosphate pathway; RFA, radiofrequency ablation; ROI, region of interest.**

Most current article

2352-345X
https://doi.org/10.1016/j.jcmgh.2022.09.009

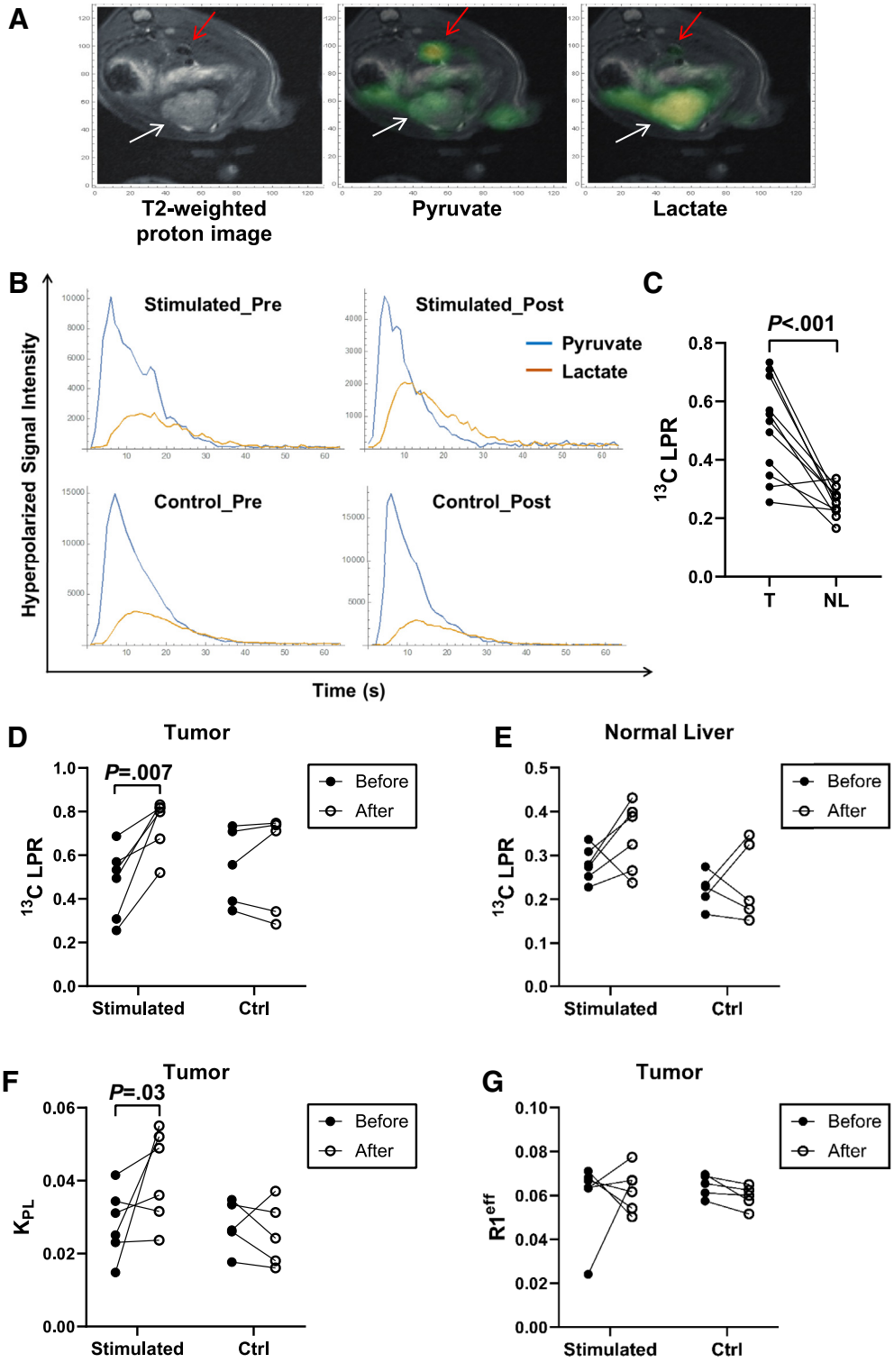

Figure 2. h^{13}C MRI of N1S1 orthotopic tumors within the left hepatic lobe of female Fischer rats. *A*, T2-weighted proton MRI (*grayscale*), with h^{13}C pyruvate (*middle panel*) and h^{13}C lactate (*right panel*) imaging overlaid in *green*, showing high lactate production within the tumor (*white arrows*) and no lactate production in kidney (*red arrows*). *B*, Example h^{13}C pyruvate and h^{13}C lactate signal over time in both control and stimulated tumors from baseline to 3 days post-stimulation/control. *C*, The baseline lactate flux in tumor (T) and normal liver (NL), expressed as LPR. *D* and *E*, LPR in tumor (*D*) and normal liver (*E*) from baseline to 3 days post-stimulation/control. *F–G*, Lactate K_{PL} (*F*) and lactate R1^{eff} (*G*) in tumor between baseline and 3 days post-stimulation/control. The *P* value was evaluated by paired *t* test.

whereas the maximum ^{13}C-lactate peak occurred at approximately 12 seconds (Figure 2, *B*). ^{13}C lactate flux was greater in N1S1 tumors compared with normal livers (lactate to pyruvate ratio [LPR] 0.51 ± 0.17 vs 0.25 ± 0.048; $P = .0006$; n = 11) (Figure 2, *C*), as well as ^{13}C-bicarbonate flux (bicarbonate to pyruvate ratio [BPR] 0.03 ± 0.02 vs 0.002 ± 0.01; $P = .0152$; n = 11) (Figure 3, *A*), whereas ^{13}C-alanine flux was lower (alanine to pyruvate ratio [APR] 0.16 ± 0.05 vs 0.27 ± 0.07; $P = .0008$; n = 11) (Figure 3, *B*). To track the evolution of the glycolytic state of N1S1 tumors following

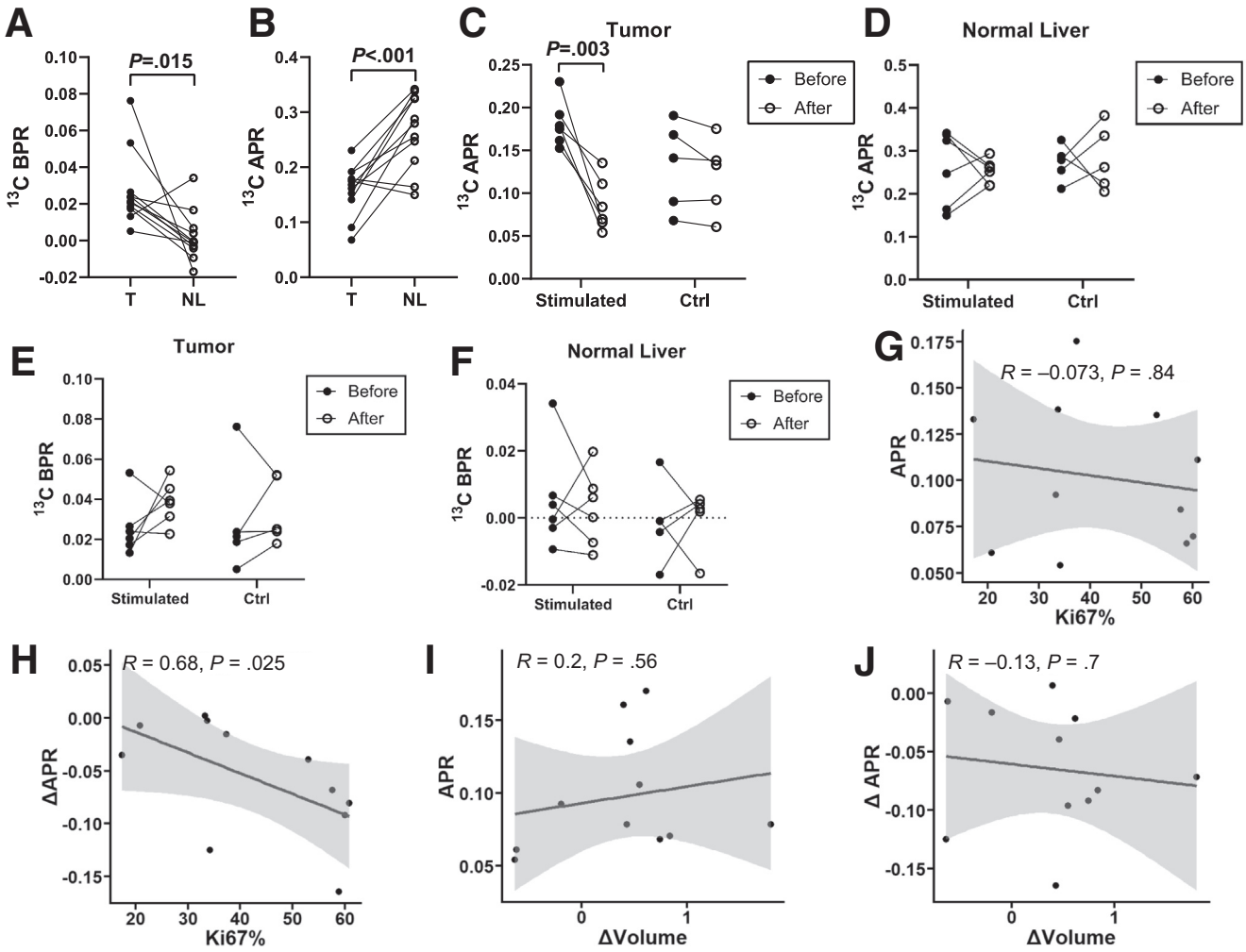

Figure 3. ^{13}C alanine and ^{13}C bicarbonate flux in N1S1 tumor. *A–B*, Bicarbonate flux (BPR) (*A*) and alanine flux (APR) (*B*). T, tumor, NL, normal liver. *C– D*, APR in tumor (*C*) and normal liver (*D*) from baseline to 3 days post-stimulation/control. *E–F*, BPR in tumor (*E*) and normal liver (*F*) from baseline to 3 days post-stimulation/control. The *P* value was evaluated by paired *t* test. *G–H*, Correlation between Ki67 expression and post-stimulation APR (*G*) or post-stimulation ΔAPR (post-stimulation APR – baseline APR) (*H*). *I–J*, Correlation between tumor volume change ΔVolume and post-stimulation APR (*I*) or post-stimulation ΔAPR (*J*).

stimulation from off-target hepatic RFA, we compared ^{13}C-lactate, ^{13}C-alanine, and ^{13}C-bicarbonate flux in HCC tumor before (baseline) and 3 days after stimulation with h^{13}C MRI. Tumor ^{13}C-lactate flux was increased in the stimulated tumors 3 days post-stimulation (LPR 0.47 ± 0.16 vs 0.74 ± 0.12; $P = .007$; n = 6) but not in controls (0.55 ± 0.18 vs 0.56 ± 0.23; $P = .67$; n = 5) (Figure 2, *D*), whereas background liver ^{13}C lactate flux was unchanged (Figure 2, *E*). Tumors also exhibited a significant decrease in ^{13}C-alanine flux from baseline to 3 days post-stimulation (APR 0.18 ± 0.03 vs 0.09 ± 0.03; $P = .003$; n = 6). In contrast, there were no changes in alanine flux in control tumors or in the adjacent normal liver tissue (Figure 3, *C–D*). ^{13}C-bicarbonate flux was no different between baseline and stimulated N1S1 tumors or within the liver parenchyma (Figure 3, *E–F*). Lactate flux as measured using K_{PL} also showed increased lactate flux in the stimulated tumors compared with controls (0.03 ± 0.01 vs 0.04 ± 0.01; $P = .03$; n = 6) (Figure 2, *F*). No change was seen in tumor $R1^{eff}$ (Figure 2, *G*).

Next, we compared the proliferation of implanted N1S1 liver tumors 3 days following stimulation. Ki67 expression was significantly greater in the stimulated group relative to control (stimulated 54.13 ± 10.14 vs control 32.82 ± 13.24; $P = .0152$; n = 6) (Figure 4, *A*). There was no difference in Ki67 expression of the background hepatic parenchyma between the RFA-stimulated or control group, confirming that the RFA-stimulation specifically affected tumor proliferation rather than globally. Mean tumor volumes did not differ at 3 days, although Ki67 expression in N1S1 tumors was positively associated with tumor volume (Figure 4, *B–C*). We then compared tumor ^{13}C-lactate and ^{13}C-alanine flux with Ki67 expression to see if imaging biomarkers were associated with tumor proliferation. Ki67 expression trended positively with ^{13}C-lactate flux measured in stimulated tumors (Figure 5, *A*), whereas there was no correlation between Ki67 expression and ^{13}C-alanine flux (Figure 3, *G*). When comparing tumor Ki67 expression with the net change in lactate or alanine flux (ΔLPR = post-stimulation

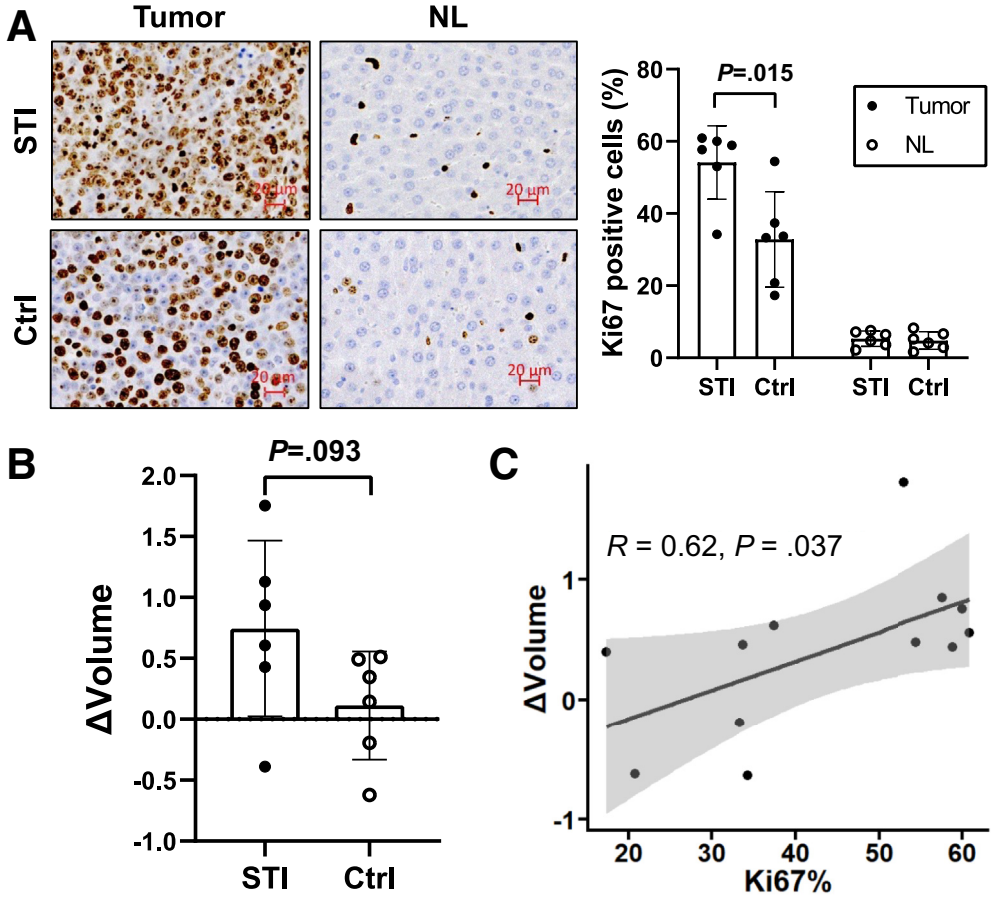

Figure 4. Stimulated normal liver by stimulation promotes HCC tumor proliferation. *A*, Ki67 expression in orthotopic tumors was examined by immunohistochemistry in both stimulated (STI) and control/sham (Ctrl) group. Representative images were provided as indicated. *B*, The volume change between baseline and 3 days post-stimulation/control (ΔVolume = $Volume_{after}$ – $Volume_{before}$) in both stimulated and control/sham group. Analyses were performed using the Mann-Whitney test. *C*, Correlation of Ki67expression and volume change.

LPR – baseline LPR, and ΔAPR = post-stimulation APR – baseline APR), Ki67 expression positively correlated with ΔLPR (Figure 5, *B*) and negatively with ΔAPR (Figure 3, *H*). Ki67 expression was also positively correlated with lactate flux as calculated with K_{PL} and net change in K_{PL} (ΔK_{PL} = post-stimulation K_{PL} – baseline K_{PL}) (Figure 5, *C–D*). Although the mean tumor volume was not significantly changed in 3 days, the volume change was positively correlated with lactate flux as calculated with LPR and K_{PL} and net change in ΔLPR and ΔK_{PL} (Figure 5, *E–H*). There was no correlation between volume change and APR or ΔAPR (Figure 3, *I–J*). These findings suggest that $h^{13}C$ MRI biomarkers, in particular, ^{13}C-lactate flux, are reflective of tumor proliferation.

Quantitative Metabolome Profiling of N1S1 Matches in vivo $h^{13}C$ MRI

We performed quantitative metabolome profiling of post-stimulated N1S1 tumors using liquid chromatography-mass spectroscopy to compare the steady-state lactate and alanine levels with their respective flux observed with $h^{13}C$ MRI. Two hundred ninety-one metabolites were detected. Multivariate analysis showed a clear separation of metabolic features for N1S1 tumors in the stimulated vs control groups (Figure 6, *A*). The Mann-Whitney *U* test was used to identify metabolites that were significantly altered in stimulated tumors as compared with control, and a heat map was generated (Figure 6, *B*). Fifty-one metabolites levels were significantly altered in stimulated tumors as compared with control, with 14 upregulated and 37 downregulated (Figure 7, *A*). Lactate levels in the stimulated tumors were elevated relative to the control group, consistent with $h^{13}C$ MRI (stimulated 1.5E-08 vs control 1.4E-08; $P = .05$; n = 9) (Figure 7, *B*). No difference was seen in alanine levels between stimulated and control groups (stimulated 4.0E-07 vs control 3.6E-07; $P = .13$; n = 9) (Figure 7, *C*).

Enrichment analysis was performed with Metaboanalyst 5.0 [27] to differentiate metabolites between stimulated tumors and controls, linking to the Kyoto Encyclopedia of Genes and Genomes metabolism pathway maps. Glycolysis/gluconeogenesis, the pentose phosphate pathway (PPP), and arginine biosynthesis were identified as major pathways (Table 1). In the glycolysis pathway, the expression levels of all intermediate metabolites of glycolysis were decreased in stimulated tumors, whereas glycolysis-produced lactate was increased (Figure 7, *D*). In the PPP, a metabolic pathway parallel to glycolysis,[28,29] 8 involved metabolites were decreased in stimulated tumors compared with controls (Figure 7, *E*). Collectively, when stimulated, the glycolysis pathway was upregulated in N1S1 tumors, while shunting metabolism towards PPP, concurrent with our observations from $h^{13}C$ MRI.

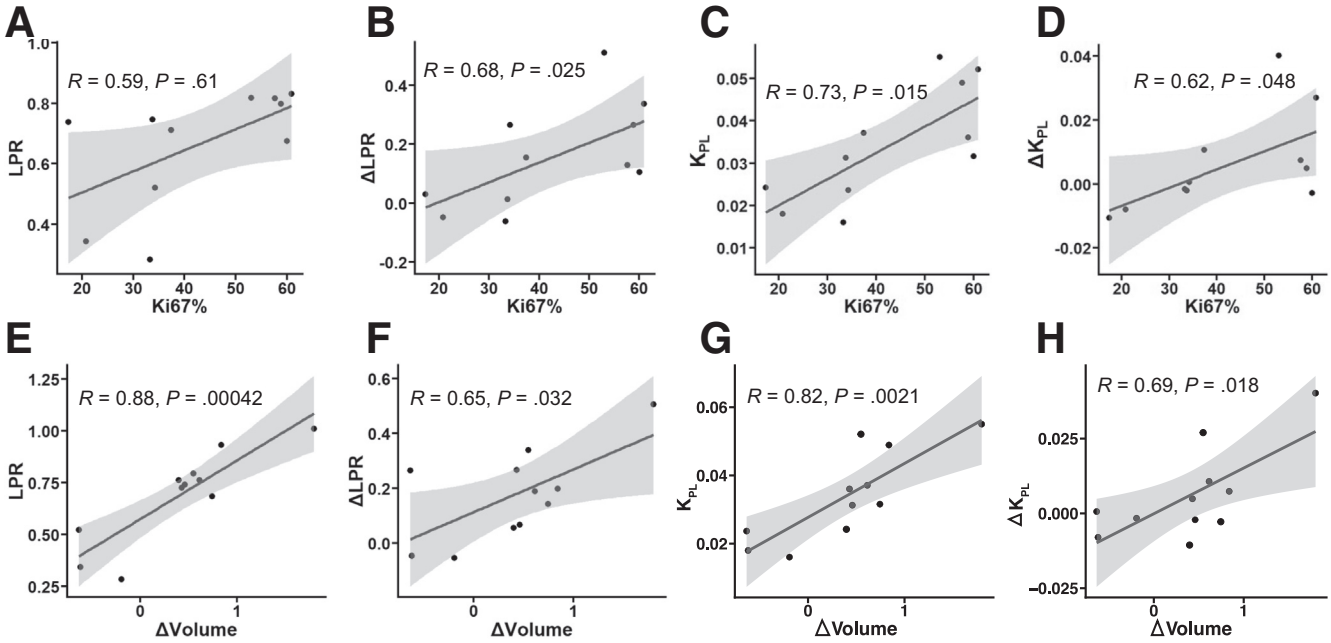

Figure 5. Correlation between tumor growth and ^{13}C-lactate flux post-stimulation. *A–B*, There is positive correlation between Ki67 expression and post-stimulation LPR and ΔLPR (post-stimulation LPR – baseline LPR). *C–D*, There is positive correlation between Ki67 expression and post-stimulation K_{PL} and ΔK_{PL} (post-stimulation K_{PL} – baseline K_{PL}). *E–F*, There is positive correlation between tumor volume change ΔVolume and post-stimulation LPR and ΔLPR. *G–H*, There is positive correlation between tumor volume change ΔVolume and post-stimulation K_{PL} and ΔK_{PL}.

Overexpression of PFKFB3 Confers Tumor Aggression Via Glycolysis

The switch from PPP to glycolysis is a common response mechanism to hypoxia in tumor cells and normal cells.[30,31] Off-target hepatic RFA induces inflammation at the periablational liver parenchyma, resulting in a global proliferative effect.[32] To elucidate the mechanisms underlying this metabolic response in tumors, we assessed the messenger RNA (mRNA) expression of several genes involved in pyruvate and lactate metabolism and transport from the harvested tumors (Figure 8, *A*). The expression of HIF-1α was significantly increased within the hepatic tissue along the rim of the ablation, also known as the periablation zone (Figure 8, *B*), simulating hypoxic-like induction. Indeed, the expression of glycolysis-related genes GLUT1, PKM, and HK2 were significantly elevated at the periablation zone and within N1S1 tumors following stimulation, concordant with HIF-1α expression (Figure 8, *C–E*). In particular, expression of PFKFB3 was significantly increased within stimulated N1S1 tumors relative to controls (Figure 9, *A*). In addition, GTP1 (gene, alanine aminotransferase 1) expression was markedly decreased at the periablation zone, corresponding

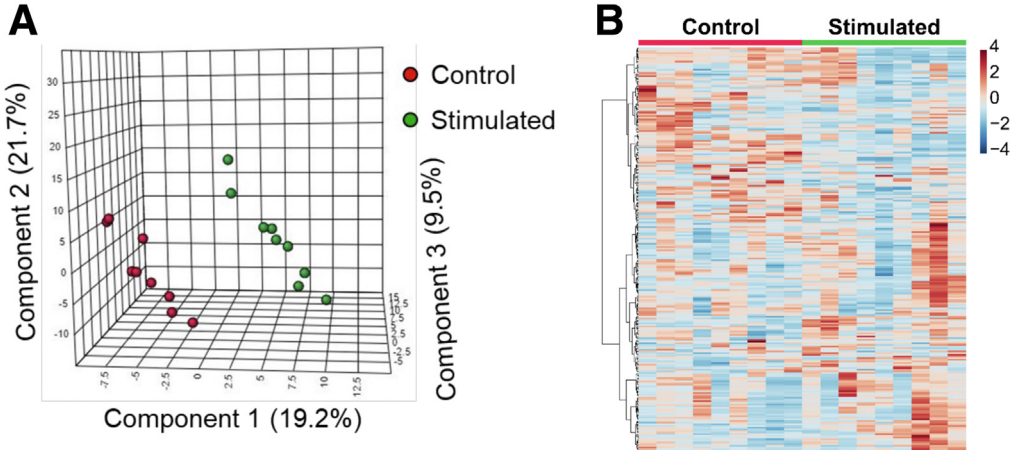

Figure 6. Metabolic profiles of N1S1 tumors. *A*, Multivariate analysis of metabolomic data using 3-D PLS-DA model. *B*, Total heat map demonstrating contrasting metabolic profiles of N1S1 tumors of control vs post-stimulated groups.

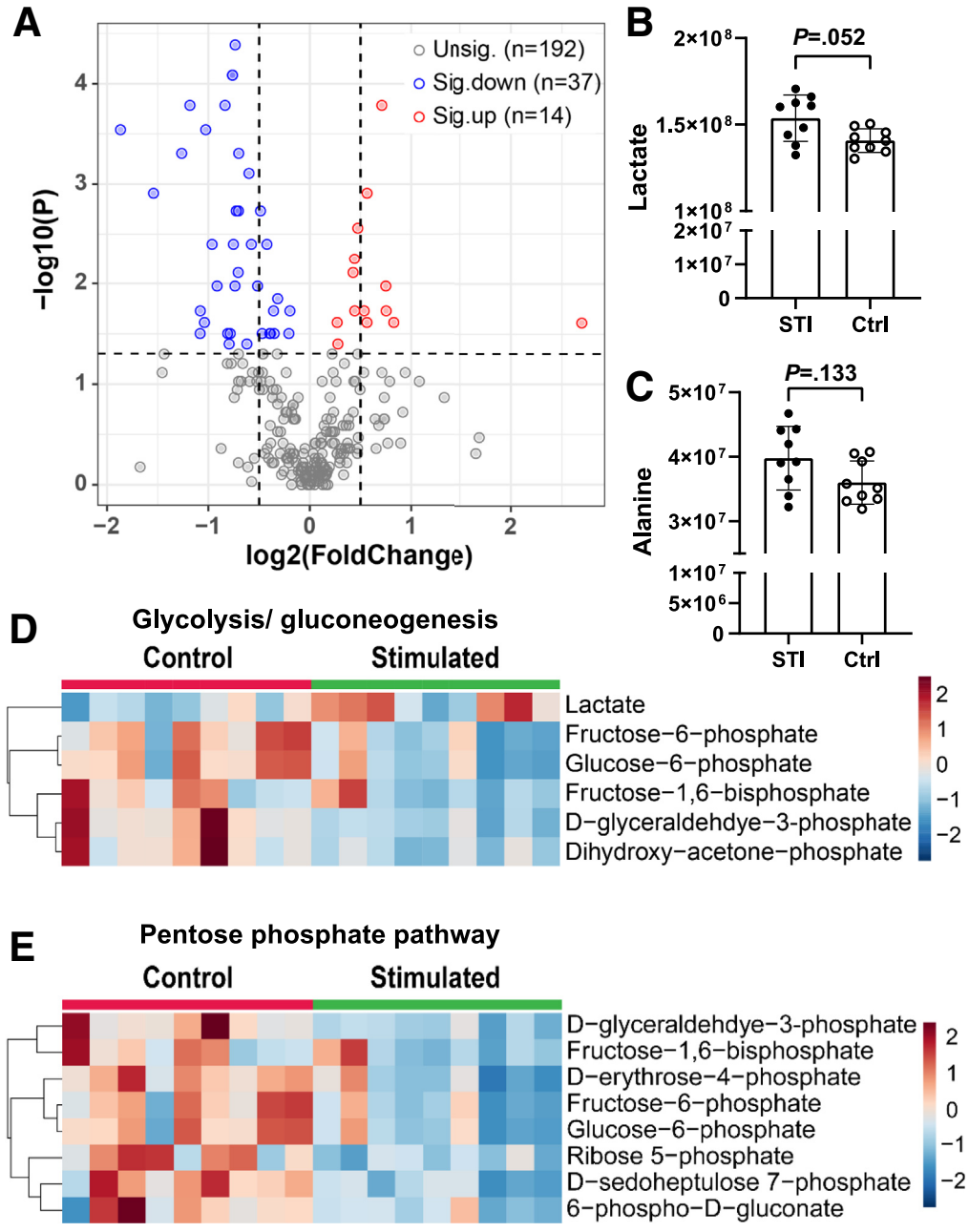

Figure 7. Quantitative metabolome profiling of post-stimulated N1S1 tumors. *A*, A volcano plot shows significantly different metabolites in stimulated tumors compared with controls. Sig.down, Metabolites significantly lower in stimulated tumor; Sig.up, metabolites significantly higher in stimulated tumor; Unsig, no difference between 2 groups. *B–C*, Lactate (*B*) and alanine levels (*C*) in stimulated (STI) tumors vs controls (Ctrl). Comparisons were made using the Mann-Whitney test. *D–E*, Focused heat maps demonstrating upregulation of glycolysis/ gluconeogenesis and downregulation of the PPP in stimulated tumors.

to deceased tumor alanine flux within stimulated tumors as measured by h^{13}C MRI (Figure 8, *F*).

The expression of PFKFB3 was also assessed by immunohistochemical staining (Figure 9, *B*), showing greater PFKFB3 production within tumors following stimulation as compared with control (Figure 9, *C*). Notably, PFKFB3 expression was markedly high at the RFA periablational zone, while absent within normal liver parenchyma (Figure 9, *D*). PFKFB3 expression in N1S1 tumors was positively correlated with Ki67 expression (Figure 9, *E*). We then compared ^{13}C lactate flux with tumor PFKFB3 expression to see if the imaging biomarkers were associated with PFKFB3 expression. Tumor PFKFB3 expression was positively correlated with both K_{PL} and ΔK_{PL}. A similar trend was seen with LPR, although not statistically significant (Figure 9, *F–I*).

PFKFB3 Inhibition With PFK15 Suppresses Glycolytic Alteration in N1S1 Tumor

With the observed the correlation between Ki67 expression and PFKFB3 in N1S1, we tested the reliance of PFKFB3 for N1S1 proliferation by assessing response of tumors from heat treatment in vitro or off-target hepatic

Table 1. Altered Metabolic Pathways Between RFA Tumor Group and Control Tumor Group

Metabolite set	*P* value	FDR
PPP	1.04E-07	8.71E-08
Ariginine biosynthesis	6.38E-04	2.56E-02
Glycolysis/gluconeogenesis	9.15E-04	2.56E-02

FDR, false discovery rate; PPP, pentose phosphate pathway; RFA, radiofrequency ablation.

RFA in vivo in combination with PFK15, a highly selective small molecule inhibitor of PFKFB3.[33,34]

To mimic the marginal zone of RFA treatment in vitro, we tested the response of N1S1 cells in response to heat stress in vitro. Annexin V-PI staining showed that N1S1 cells exposed to 45 °C for 5 minutes resulted in 80.9% survival after 24 hours without signs of apoptosis, vs 34.3% at 50 °C, and 0% at 55 °C (Figure 10, *A*). Three to 10 days following heat treatment, the proliferation rate of N1S1 within the 50 °C-treated group was significantly greater compared with the controls at 37 °C (2-way analysis of variance [ANOVA], 48 hours $P = .0004$; 72 hours $P < .0001$) (Figure 10, *B*). Heat-treated N1S1 cells in vitro demonstrated increased cellular proliferation measured by MTT assay without PFK15 or at low doses (1 nmol/L and 2 nmol/L), with greater proliferation at 45 °C and 50 °C as compared with controls at 37 °C (2-way ANOVA, 1 nmol/L 37 °C vs 45 °C $P = .02$; 37 °C vs 50 °C $P = .002$; 2 nmol/L 37 °C vs 50 °C $P = .008$). However, at effective concentrations of PFK15 at 10 nmol/L, N1S1 proliferation was suppressed at all 3 temperatures (Figure 10, *C*).

In vivo $h^{13}C$ MRI showed the LPR and K_{PL} were elevated after stimulation, whereas the increase of LPR and K_{PL} was inhibited by PFK15 administration (Figure 11, *A–B*). PFK15 suppressed the elevation of PFKFB3 in N1S1 tumors following stimulation in both mRNA level and protein level (Figure 11, *C–D*). Taken together, these results suggest that PFK15 can suppress glycolysis upregulation, supporting the notion that PFKFB3 may be a treatment target for HCC.

Discussion

Metabolic reprogramming is a characteristic feature of cancer cells, and in cancers, metabolic pathways may undergo alterations constantly.[35] Enhancement of glycolysis and lactate accumulation in the interstitial space primarily serves the purpose of building and preserving a protumorigenic environment,[36,37] suggesting that lactate signaling maybe serve as an early indicator for disease progression. Prior studies have supported the safety and feasibility of in vivo $h^{13}C$ MRI, with the real-time pyruvate, lactate, and alanine signal detectable in different tissues, including prostate, liver, kidney, and brain.[15] In this study, we used $h^{13}C$ MRI to assess HCC metabolism and found a strong correlation between measured in vivo lactate flux and tumor proliferation before detectable volumetric change. $h^{13}C$ MRI may therefore provide a noninvasive way

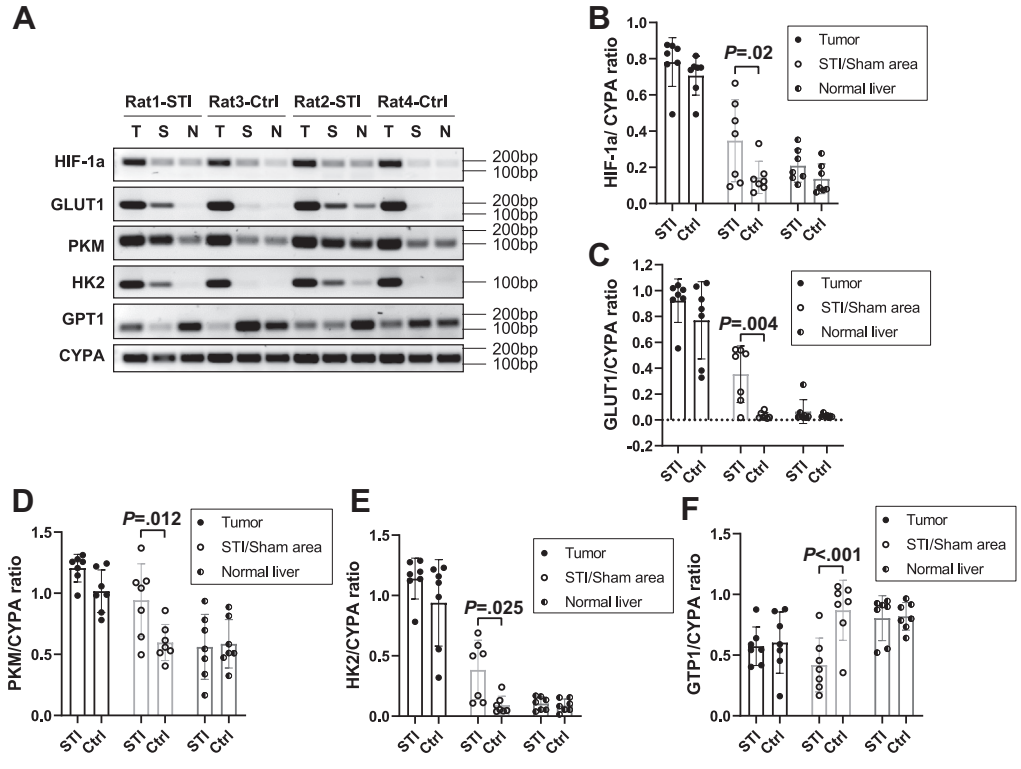

Figure 8. mRNA expression of glycolysis-related genes in stimulated/nonstimulated N1S1 tumors and liver tissue. *A*, Representative gene expression patterns in tumor (T), liver tissue adjacent to RFA/sham site (periablational) (P), and normal liver (N). *B–F*, Relative HIF-1 (*B*), GLUT1 (*C*), PKM (*D*), HK2 (*E*), and GPT1 (*F*) gene expression levels within tumor, periablational, and normal liver, in stimulated (STI) and control (Ctrl) groups. Densitometry quantification of band intensity is presented as a percentage of relative densitometry normalized to the CYPA gene. Analyses were performed using 2-way ANOVA.

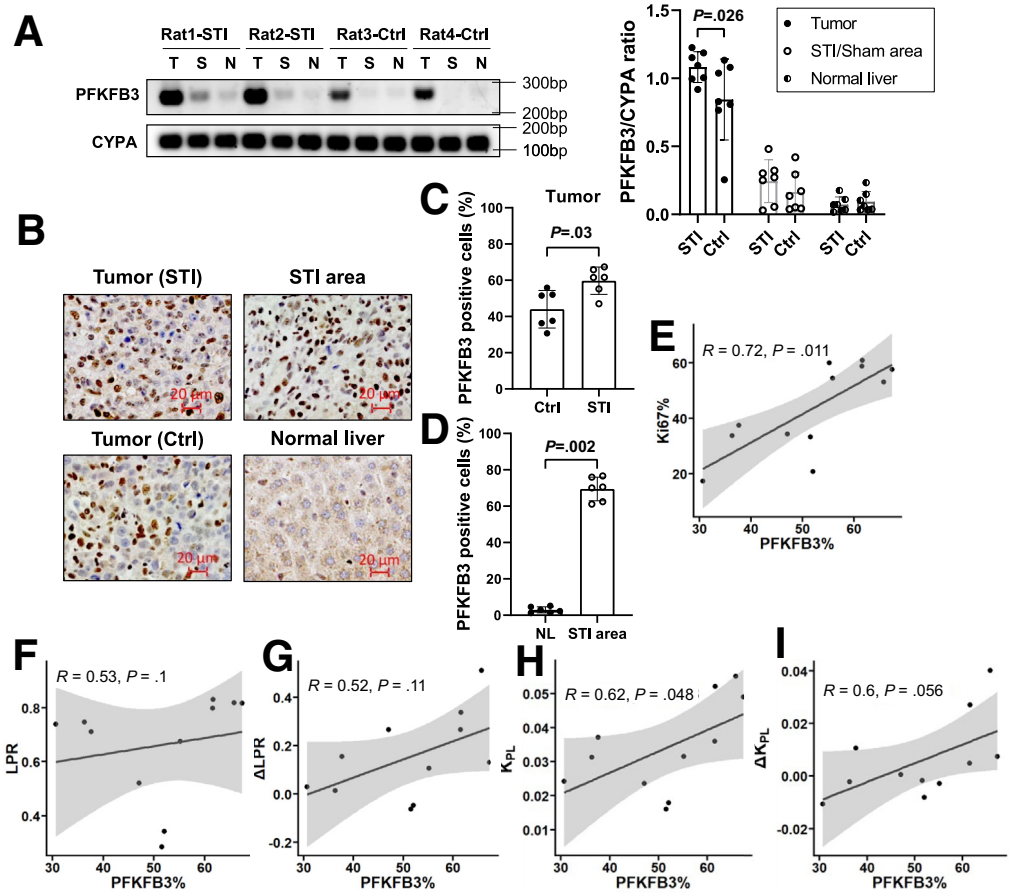

Figure 9. PFKFB3 expression in N1S1 tumors. *A*, Representative gene expression patterns in tumor (T), stimulated or nearby sham liver tissue (S), and normal liver (N). PFKFB3 gene expression levels in stimulated (STI) and control (Ctrl) groups. Densitometry quantification of band intensity is presented as a percentage of relative densitometry normalized to the cyclophilin A (CYPA) gene. Analyses were performed using 2-way ANOVA. *B–D*, PFKFB3 immunohistochemistry staining demonstrating different levels of expression within tumor, stimulated/sham area, and normal liver. Quantitative immunohistochemistry analysis in tumors (*C*), and stimulated area (STI area), and normal liver (NL) (*D*). Analyses were performed using the Mann-Whitney test. *E–I*, Correlation PFKFB3 expression with Ki67 (*E*), post-stimulated LPR (*F*), ΔLPR (*G*), post-stimulated lactate K_{PL} (*H*) or ΔK_{PL} (*I*).

to obtain earlier insight into transformation of tumors into a higher grade.

Using a model of stimulated HCC, we found that increased lactate flux in HCC tumors was detectable in vivo by $h^{13}C$ MRI 3 days after stimulation, correlating with proliferation as detected by Ki67 expression, ahead of changes in tumor volume which are detectable only at a later time. Meanwhile, the effective lactate relaxation ($R1^{eff}$), a product of MR parameters such as flip angle and T1 relaxation, remained unchanged, confirming that the changes in measured lactate flux were not due to technical variations such as surface coil inhomogeneity.

The metabolic phenotype of cancer cells changes in response to shifting levels of oxygen and nutrients during growth.[38,39] Glycolysis and PPP are parallel metabolic pathways that catalyze glucose and support cell survival and proliferation. In this study, we showed that tumor aggressiveness was associated with a shift towards aerobic glycolysis and downregulation of PPP in N1S1 HCC tumors. Hypoxia is known to induce a similar shift towards glycolysis in a broad spectrum of cancer and nonneoplastic cells.[30] This shift, coupled with increased glucose uptake, is used by proliferating cells to convert macromolecules needed to construct new cells.[9,40]

Glucose metabolism consists of highly interconnected pathways, and the one of the key junction biomolecules between glycolysis and PPP is glucose-6-phosphate. Upon entering cells, glucose is rapidly phosphorylated to glucose-6-phosphate and subsequently metabolized towards glycolysis or the PPP. PFKFB3 is involved in this commitment towards glycolytic flux. Its product, fructose-2,6-bisphosphate, is a known potent allosteric activator of 6-phosphofructo-1-kinase, which in turn catalyzes commitment to glycolysis.[41] PFKFB3 overexpression has been detected in several different tumor cells as well as various cells within the tumor microenvironment, and plays an important part in oncogenesis and the survival and proliferation of cancer cells.[42,43] In our study, PFKFB3 expression was increased in stimulated N1S1 tumors. PFKFB3 expression was also associated with lactate flux as measured by

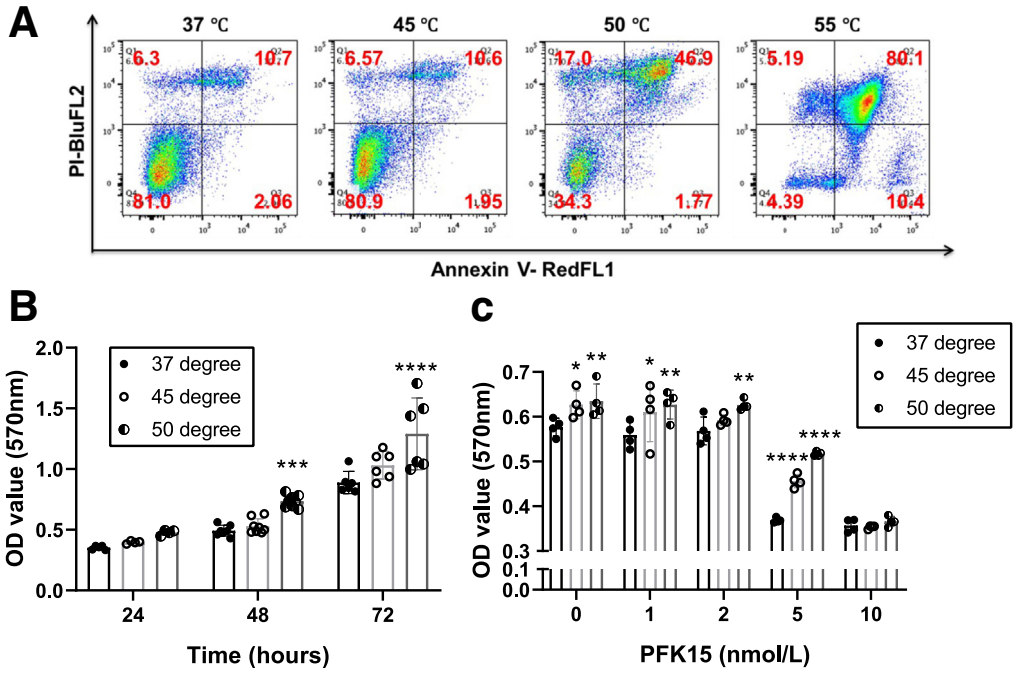

Figure 10. PFK15 inhibits N1S1 cell viability. *A*, Flow cytometric dotplot analysis of Annexin V/PI staining in heat-treated cells 2 days following heat treatment. *B*, Cellular proliferation was measured by the MTT assay in heat-treated cells at 24 hours, 48 hours, and 72 hours. Values are expressed as mean and standard deviation. *C*, Cell viability was measured by the MTT assay in heat-treated cells treated with the indicated concentrations of PFK15 for 72 hours. Values are expressed as mean and standard deviation. **P* < .05; ***P* < .01; ****P* < .001; *****P* < .0001; compared with the 37 °C group. Analyses were performed using 2-way ANOVA.

$h^{13}C$ MRI, suggesting $h^{13}C$ MRI may guide the use of PFKFB3 inhibitors as an alternative or adjunct therapy. This is supported by our in vitro and in vivo studies where PFKFB was directly inhibited with PFK15, resulting in the suppression of proliferation and MRI-measured lactate flux in stimulated tumors. PFKFB3 may therefore be a potential therapeutic target in HCCs where glycolysis is the primary metabolic driver. However, glycolytic suppression may be compensated effectively by alternate pathways. Indeed, the PPP and glycolysis share glucose-6-phosphate such that increased glycolysis during reperfusion concomitantly leads to decreased dependency on the PPP.[30] PFKFB3 inhibition has also been shown to redirect glucose from the glycolysis pathway to the PPP, which can lead to treatment resistance.[44] Future studies are needed to see if this occurs and if concurrent PPP blockade may enhance therapeutic response.

Interestingly, alanine flux detected by $h^{13}C$ MRI was significantly lower in HCC tumor compared with normal liver, with a further significant decrease following stimulation. Our MRI results are concordant with a previous $h^{13}C$ MRI study, which reported absence of alanine flux in normal liver tissues, significantly increased alanine flux in precancerous tissues, and decreased alanine flux in established liver tumors.[45] However, our measured change in tumor alanine flux following stimulation did not correlate with Ki67 expression and was not matched by the ex vivo metabolomics analysis. This can be explained by the fact that alanine levels measured by $h^{13}C$ MRI reflect conversion from injected pyruvate taken into the tumor cells, whereas the absolute value of alanine detected by mass spectroscopy does not discriminate the source, which can be exogenous (eg, muscle). This notion is supported by studies that have shown that exogenous alanine may be used as an alternative metabolic pathway.[46]

In this study, we showed that N1S1 HCC proliferation is associated with a shift towards aerobic glycolysis and downregulation of PPP via up-regulation of PFKFB3 expression, with the corresponding glycolytic changes detectable by $h^{13}C$ MRI.

Materials and Methods

N1S1 Cell Line

The rat hepatocellular carcinoma cell line N1S1 (ATCC, CRL-1604™, male) was obtained from ATCC (Manassas, VA). Cells were maintained at 37 °C in a humidified atmosphere with 5% CO2 and grown in Iscove's Modified Dulbecco's Medium (GIBCO) and 1% antibiotic-antimycotic (100×) (GIBCO).

Animal Models

Animal studies were performed under a protocol approved by the institutional animal care and use committee, in accordance with the guidelines of the Institute of Laboratory Animal Resources, National Research Council. The 2 rats were housed in a temperature-controlled (22 ± 1°C) animal facility with a 12-hour light/dark cycle. The

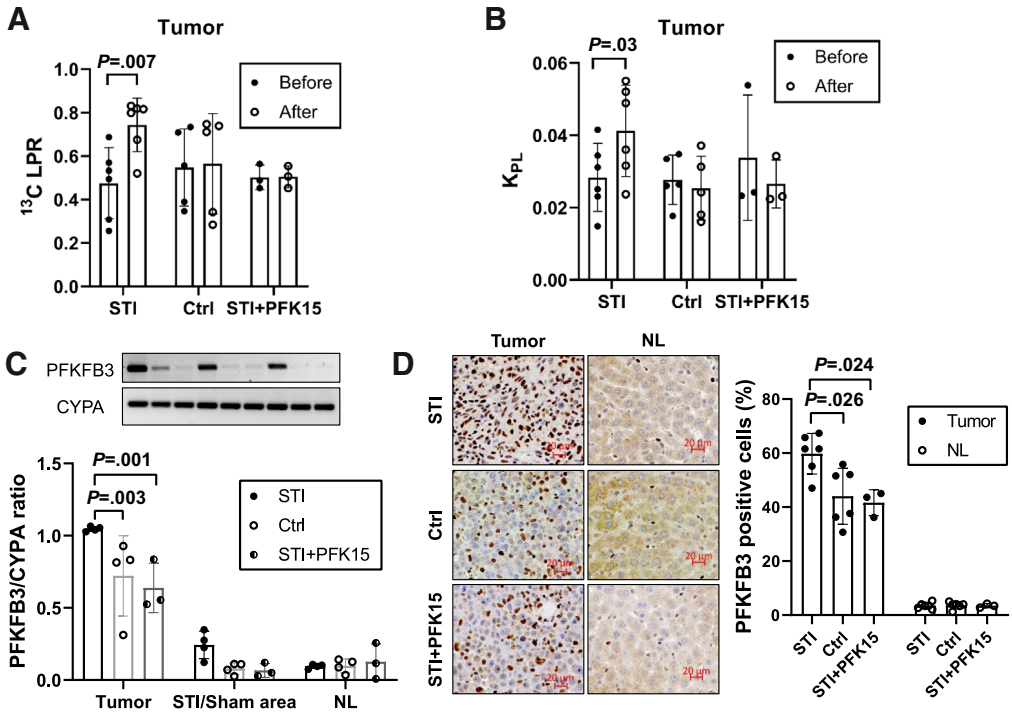

Figure 11. Inhibition of PFKFB3 in N1S1 with PFK15. *A–B*, The lactate flux (*A*) and lactate K_{PL} (*B*) in control (Ctrl), stimulated (STI), and stimulation with PFK15 (STI+PFK15) group. The *P* value was evaluated by paired *t* test. *C*, PFKFB3 gene expression levels within tumor, stimulated area/sham liver tissue (STI/Sham area), and normal liver (NL). Densitometry quantification of band intensity is presented as a percentage of relative densitometry normalized to the cyclophilin A (CYPA) gene. Analyses were performed using 2-way ANOVA. *D*, Immunohistochemistry shows PFKFB3 expression in tumor and normal liver. Analyses were performed using the Mann-Whitney test.

general health of the rats was monitored daily for any signs of suffering or abnormal behavior.

A total of 15 adult female Fischer (CDF) rats (Charles River, Germantown, MD) weighing 120 to 150 g were used in this study. N1S1 cells (10^6/50 μl) were implanted into left hepatic lobe of rats. When tumors reached 8 to 10 mm, 12 rats were randomized into sham (control) group vs stimulated group (6 each).

All rats underwent laparotomy, which was performed under anesthesia using aseptic techniques. The right hepatic lobe was exposed, and a radiofrequency probe was placed on the liver surface. RFA (stimulated) or sham (control) was then performed at the surface of the right hepatic lobe (see next section). h^{13}C MRI was performed prior to RFA/sham (baseline) and 72 hours post-RFA/sham.

All tumors were harvested immediately after the final h^{13}C MRI study (ie, 3 days post-stimulation/sham) and stored at −80 °C for histologic, metabolomic, and mRNA analysis.

Radiofrequency Ablation and Sham Procedures

A monopolar RFA generator (500 kHz RF generator, Radionics, Model CC-1) was used to energize the probe tip at 70 °C for 5 minutes while it rested on the surface of the right hepatic lobe. In sham procedures performed on control rats, all the steps of RFA were performed, including resting of the probe on the liver surface for 5 minutes, except the probe was not energized.

Hyperpolarized ^{13}C MRI

Rats were anesthetized with isoflurane (4% induction, 2.5%–3 % maintenance) with oxygen (700 mL/minute) and the breathing rate was maintained at 80 ± 15 breaths per minute. Core body temperature was maintained at 36 ± 1 °C with a feedback-controlled warm air circulator equipped with a fiber-optic temperature probe. The lateral tail vein was cannulated with a 24-gauge flexible catheter connected an 84-cm extension tube with 0.5 mm inside diameter (SAI Infusions, Lake Villa, IL). Hyperpolarized ^{13}C pyruvate solution was prepared by dynamic nuclear polarization using a commercial polarizer (Hypersense, Oxford Instruments Molecular Biotools). [1-^{13}C] pyruvic acid was combined with 15 mM OX063 radical (GE Healthcare, London, UK) and 1 mM gadoteridol (ProHance, Bracco, Milan, Italy) and polarized for 40 minutes or more at 1.4 K and 100 mW microwave power. The hyperpolarized material was then dissolved in saline containing 50 mM TRIS and 125mg/L EDTA and adjusted to physiological pH with sodium hydroxide to obtain a 96 mM hyperpolarized pyruvate solution. A total of 2.5 mL was administered via tail vein as a bolus injection lasting approximately 10 seconds. Imaging was performed on a 9.4-T small animal MRI (Biospec 94/20, Bruker) with an 84-mm quadrature proton coil and an in-house built transmit/receive ^{13}C surface coil built on a 65-mm cylindrical form with an axial length of 60 mm and a circumferential width of 50 cm. Animals were carefully

situated with tumors within 5 mm of the center of the coil during imaging to minimize the effects of the surface coil sensitivity profile. ^{13}C data were acquired in the axial plane across the middle of the tumor using an echo planar spectroscopic imaging non-gated sequence with a 4° tip angle, 16 × 16 matrix, 4.5 × 4.5 cm field of view, 6 to 9 mm slice thickness, 512 spectral points, and 4 kHz spectral width. Sixty-four repetitions were acquired with 2.16 seconds temporal resolution. Echo planar spectroscopic imaging was initiated immediately prior to infusion of pyruvate solution to enable measurement of the entire time course of the pyruvate and lactate/alanine signals. A [1-^{13}C] acetate phantom was placed adjacent to the animal on the opposite side of the surface coil. The chemical shift of acetate is approximately 0.5 ppm from lactate, enabling ready identification of pyruvate and lactate. The chemical shift assignments were confirmed by observing the large intravascular ^{13}C signal, which at early time points is dominated by pyruvate.

Conventional ^{1}H MRI was performed every 5 days to track tumor growth using the same magnet, with an 84 mm quadrature coil. T2-weighted axial, coronal, and sagittal sequences were acquired using the rapid imaging with refocused echoes sequence with the following parameters: 6 cm field of view, 128 × 128 matrix, echo train length of 8, TR 1245 ms, TE 11 ms, 2 mm slice thickness.

To quantify ^{13}C-pyruvate to ^{13}C-lactate, ^{13}C-alanine, and ^{13}C-bicarbonate flux, we integrated across each spectral peak and across all time points within a manually drawn region of interest using the ^{1}H anatomical images as guidance. Lactate, alanine, and bicarbonate flux were measured as the ratio of the integrated signal of each species relative to pyruvate, expressed as LPR, APR, and BPR, respectively.

MRI Reconstruction and Analysis

Spectroscopic image data were separated into even and odd echoes, apodized with a 30-Hz line-broadening filter and reconstructed with standard Fourier methods to obtain pixel-by-pixel spectra with 2 kHz spectral width. Spectra from even and odd echoes were then combined after application of a first-order phase to account for the temporal offset between the starting points of the 2 echo trains. Pixel-by-pixel magnitude spectra were computed, and metabolite signals were quantified by integrating their spectral peaks, after subtracting the mean magnitude noise from the spectra to eliminate spurious baseline signals. Magnitude noise was estimated from a noise-only spectrum. Metabolite images were resized to 128-by-128 matrices by zero fill interpolation and matched to the anatomical proton images. Regions of interest (ROIs) covering the tumors were drawn on the anatomical proton images, and metabolite signals were obtained from the sum of the pixel intensities over the ROIs in the resized ^{13}C images. An ROI was drawn within the right hepatic lobe (the tumors having been implanted in the left lobe) to obtain background liver measurements. LPRs were computed using the time integrals of each metabolite's signal, a measure that has been shown to reflect the rate of label exchange between pyruvate and lactate.[47] This analysis was repeated to compute the APR and the BPR.

Kinetic modeling of lactate formation was performed fitting the measured lactate and pyruvate time courses to a simplified 2-site exchange model. In the model, the lactate signal $L(t)$ is determined from the pyruvate signal $P(t)$ in terms of a forward rate constant k_{PL} and an effective decay rate R_1^{eff} according to

$$\frac{dL(t)}{dt} = k_{PL}P(t) - R_1^{eff}L(t)$$

where R_1^{eff} includes the effects of tracer outflow, T_1 decay, and saturation by RF pulses. This equation was solved by standard methods using the measured pyruvate signal, and the parameters k_{PL} and R_1^{eff} were determined by a least-squares fit of this solution to the measured lactate signal.

Stimulated N1S1 and PFKFB3 Suppression With PFK15

An additional 3 rats were implanted with N1S1 in the same fashion as detailed above, and when tumors reached 8 to 10 mm, these rats were treated with the same protocol as for the stimulated group (right hepatic lobe RFA) with the addition of treatment with PFK15 using a previously-established dose (Selleck, 25 mg/kg intraperitoneal).[33,34] As with the other rats, h^{13}C MRI was performed at baseline and again 72 hours post-stimulation.

In Vitro Heat Treatment Assays

Suspended N1S1 cells were collected in a 15 mL tube in 3 mL of medium (5 × 10^5 cells), and immediately exposed to 37 °C, 45 °C, 50 °C, 55 °C, 60 °C, and 70 °C water-bath for 5 minutes. Cells were then seeded into 75-cm^2 cell-culture flasks in 18 mL of Iscove's Modified Dulbecco's Medium and maintained at 37 °C.

For cell death analysis, cells were harvested and washed once with phosphate buffered saline, and then resuspended in PI/Annexin-V solution (ab176749, Abcam) for apoptosis analysis. At least 10,000 cells were analyzed on a FACSCalibur flow cytometer (Becton Dickinson). Data were analyzed by using FlowJo software.

For in vitro proliferation measurements, N1S1 (10^3 cells/well) from each of the different heat-treated groups were plated in 96-well cell culture plates. After 2 to 5 days, 10 μL MTT (M5655, Sigma, 5 mg/mL, 3-(4,5-Dimethylthiazol-2-yl)-2,5-diphenyltetrazolium bromide) were added to each well, incubated for 4 hours at 37 °C, and 150 μL of DMSO (BP231-100, Fisher Scientific) were then added to each well to dissolve the crystal formazan dye. Absorbance was measured at 570 nm on an enzyme-linked immunosorbent assay reader. For relative quantification, the value of absorbance in each group was normalized to that in the 37 °C group.

Quantitative Polar Metabolomic Profiling

Metabolomics analyses were performed at the mass spectrometry (proteomics/metabolomics) core facility. Tumor xenografts were extracted immediately after the last

Table 2. Primer Sequences

Gene	Forward (5' to 3')	Reverse (5' to 3')
CYPA	TATCTGCACTGCCAAGACTGAGTG	CTTCTTGCTGGTCTTGCCATTCC
HIF-1α	TGCTTGGTGCTGATTTGTGA	GGTCAGATGATCAGAGTCCA
PFKFB3	TTGGTCATCTGTCACCAGGC	GCGGACTCCACAGACAGAAA
GLUT1	GCTGTGGCTGGCTTCTCTAA	CCGGAAGCGATCTCATCGAA
PKM	TCATCAGCAAAATCGAGAACCA	CCACGAGCTACCATGATTCCA
HK2	TCAGCCCAGAACTCCTTACCA	CGATTCCATCCTTATCCTCTTCA
GPT1	AGGACAACGTGTATGCCGAG	CTCGCCCATGTAGCCCTTAG

CYPA, Cyclophilin A; HIF-1a, hypoxia-inducible factor 1-alpha; PFKFB3, 6-phosphofructo-2-kinase/fructose-2,6-bisphosphatase-3; GLUT1, glucose transporter 1; PKM, pyruvate kinase M; HK2, hexokinase 2; GPT1, alanine aminotransferase 1.

$h^{13}C$ MRI examination and kept at liquid nitrogen until extraction, and metabolites were extracted according to an established protocol.[48] Data were analyzed by R (RStudio software).

Total RNA Extraction, cDNA Synthesis, and Quantitative RT-PCR (RT-qPCR)

Frozen rat tissues (including tumor, ablation zone, and normal liver) were ground with a pestle in liquid nitrogen to obtain homogeneous tissue powder. Cells were collected and washed with phosphate buffered saline. Total RNA was extracted from the tissue powder or cell pellets using the RNeasy Mini kit (74134, Qiagen) and reverse transcribed into cDNA using iScript gDNA Clear cDNA Synthesis Kit (1725035, BIO-RAD). The level of mRNA expression was normalized to the housekeeping gene cyclophilin A. The mRNA expression of HIF-1α, GLUT1, HK2, PFKFB3, PKM, and GPT1 were measured. The primer sequences are listed in Table 2.

Histologic Analysis

Liver tissue samples were fixed in 10% neutral formalin and paraffin-embedded section were stained with hematoxylin and eosin to analyze the histology of samples. Immunohistochemistry staining was performed on paraffin-embedded liver tissue sections. We used the following primary antibodies: PFKFB3 (NOVUS Biologicals, NBP2-75393, 1:200) and Ki67 (Cell Signaling, CST12202S, 1:1000). Staining was visualized using Goat anti-Rabbit IgG (Abcam, ab214880) conjugated with HRP polymer and 3,3-diaminobenzidine (Vector lab). Slides were scanned on an Axio Scan.Z1 (Zeiss) and the whole mount digitalized at 10× magnification. Three regions in each sample were randomly selected and analyzed using ImageJ.

Statistical Analysis

Statistical analysis was performed using Prism 9 (GraphPad). Comparisons between $h^{13}C$ MRI and Ki67 measurements were made using linear regression. Comparisons between pre-treatment and post treatment, and comparisons between 2 tissues from the same subject were made using the paired *t* test. Comparisons between different treatment groups were made using the Mann-Whitney test. For in vitro experiments, analyses were performed using 2-way ANOVA. Data are deemed to be statistically significant for $P < .05$. Errors are reported as standard error of means unless otherwise indicated.

References

1. Ghouri Y, Mian I, Rowe J. Review of hepatocellular carcinoma: epidemiology, etiology, and carcinogenesis. J Carcinog 2017;16:1.
2. Llovet JM, Villanueva A, Lachenmayer A, Finn RS. Advances in targeted therapies for hepatocellular carcinoma in the genomic era. Nat Rev Clin Oncol 2015;12:408–424.
3. Amann T, Maegdefrau U, Hartmann A, Agaimy A, Marienhagen J, Weiss TS, Stoeltzing O, Warnecke C, Schölmerich J, Oefner PJ, Kreutz M, Bosserhoff AK, Hellerbrand C. GLUT1 expression is increased in hepatocellular carcinoma and promotes tumorigenesis. Am J Pathol 2009;174:1544–1552.
4. Calvisi DF, Wang C, Ho C, Ladu S, Lee SA, Mattu S, Destefanis G, Delogu S, Zimmermann A, Ericsson J, Brozzetti S, Staniscia T, Chen X, Dombrowski F, Evert M. Increased lipogenesis, induced by AKT-mTORC1-RPS6 signaling, promotes development of human hepatocellular carcinoma. Gastroenterology 2011;140:1071–1083.
5. Suzuki H, Kohjima M, Tanaka M, Goya T, Itoh S, Yoshizumi T, Mori M, Tsuda M, Takahashi M, Kurokawa M, Imoto K, Tashiro S, Kuwano A, Kato M, Okada S, Nakamuta M, Ogawa Y. Metabolic alteration in hepatocellular carcinoma: mechanism of lipid accumulation in well-differentiated hepatocellular carcinoma. Can J Gastroenterol Hepatol 2021;2021:8813410.
6. Pavlova NN, Thompson CB. The emerging hallmarks of cancer metabolism. Cell Metab 2016;23:27–47.
7. Tenen DG, Chai L, Tan JL. Metabolic alterations and vulnerabilities in hepatocellular carcinoma. Gastroenterol Rep 2021;9:1–13.
8. Sengupta D, Pratx G. Imaging metabolic heterogeneity in cancer. Mol Cancer 2016;15:4.
9. Vander Heiden MG, Cantley LC, Thompson CB. Understanding the Warburg effect: the metabolic requirements of cell proliferation. Science 2009;324:1029–1033.

10. Romero-Garcia S, Moreno-Altamirano MMB, Prado-Garcia H, Sánchez-García FJ. Lactate contribution to the tumor microenvironment: mechanisms, effects on immune cells and therapeutic relevance. Front Immunol 2016;7:52.
11. Zhang H. The potential of hyperpolarized 13C MRI in assessing signaling pathways in cancer. Acad Radiol 2014;21:215–222.
12. Darpolor M, Yen Y-F, Chua M-S, Xing L, Clarke-Katzenberg R, Shi W, Mayer D, Josan S, Hurd R, Pfefferbaum A, Senadheera L, So S, Hofmann L, Glazer G, Spielman D. In vivo MRSI of hyperpolarized [1-13C]pyruvate metabolism in rat hepatocellular carcinoma. NMR in Biomed 2011;24:506–513.
13. Perkons NR, Kiefer RM, Noji MC, Pourfathi M, Ackerman D, Siddiqui S, Tischfield D, Profka E, Johnson O, Pickup S, Mancuso A, Pantel A, Denburg MR, Nadolski GJ, Hunt SJ, Furth EE, Kadlecek S, Gade TPF. Hyperpolarized metabolic imaging detects latent hepatocellular carcinoma domains surviving locoregional therapy. Hepatology 2020;72:140–154.
14. Albers MJ, Bok R, Chen AP, Cunningham CH, Zierhut ML, Zhang VY, Kohler SJ, Tropp J, Hurd RE, Yen Y-F, Nelson SJ, Vigneron DB, Kurhanewicz J. Hyperpolarized 13C lactate, pyruvate, and alanine: noninvasive biomarkers for prostate cancer detection and grading. Cancer Res 2008;68:8607–8615.
15. Granlund KL, Tee S-S, Vargas HA, Lyashchenko SK, Reznik E, Fine S, Laudone V, Eastham JA, Touijer KA, Reuter VE, Gonen M, Sosa RE, Nicholson D, Guo YW, Chen AP, Tropp J, Robb F, Hricak H, Keshari KR. Hyperpolarized MRI of human prostate cancer reveals increased lactate with tumor grade driven by monocarboxylate transporter 1. Cell Metab 2020;31:105–114.e3.
16. Lam VW-T, Ng KK-C, Chok KS-H, Cheung T-T, Yuen J, Tung H, Tso W-K, Fan S-T, Poon RT. Risk factors and prognostic factors of local recurrence after radiofrequency ablation of hepatocellular carcinoma. J Am Coll Surg 2008;207:20–29.
17. Ahmed M, Kumar G, Moussa M, Wang Y, Rozenblum N, Galun E, Goldberg SN. Hepatic radiofrequency ablation-induced stimulation of distant tumor growth is suppressed by c-Met inhibition. Radiology 2016;279:103–117.
18. Rozenblum N, Zeira E, Scaiewicz V, Bulvik B, Gourevitch S, Yotvat H, Galun E, Goldberg SN. Oncogenesis: an "off-target" effect of radiofrequency ablation. Radiology 2015;276:426–432.
19. Yamada S, Utsunomiya T, Morine Y, Imura S, Ikemoto T, Arakawa Y, Kanamoto M, Iwahashi S, Saito Y, Takasu C, Ishikawa D, Shimada M. Expressions of hypoxia-inducible factor-1 and epithelial cell adhesion molecule are linked with aggressive local recurrence of hepatocellular carcinoma after radiofrequency ablation therapy. Ann Surg Oncol 2014;21(Suppl 3):S436–S442.
20. Wan J, Ling X, Rao Z, Peng B, Ding G. Independent prognostic value of HIF-1[alpha] expression in radiofrequency ablation of lung cancer. Oncol Lett 2020;19:849–857.
21. Wan J, Wu W, Zhang R. Local recurrence of small cell lung cancer following radiofrequency ablation is induced by HIF-1α expression in the transition zone. Oncol Rep 2016;35:1297–1308.
22. Denko NC. Hypoxia, HIF1 and glucose metabolism in the solid tumour. Nat Rev Cancer 2008;8:705–713.
23. Minchenko A, Leshchinsky I, Opentanova I, Sang N, Srinivas V, Armstead V, Caro J. Hypoxia-inducible factor-1-mediated expression of the 6-phosphofructo-2-kinase/fructose-2,6-bisphosphatase-3 (PFKFB3) gene. Its possible role in the Warburg effect. J Biol Chem 2002;277:6183–6187.
24. Ikemoto T, Shimada M, Yamada S. Pathophysiology of recurrent hepatocellular carcinoma after radiofrequency ablation. Hepatol Res 2017;47:23–30.
25. Ng KK, Poon RT, Lo C-M, Yuen J, Tso WK, Fan S-T. Analysis of recurrence pattern and its influence on survival outcome after radiofrequency ablation of hepatocellular carcinoma. J Gastrointest Surg 2008;12:183–191.
26. Velez E, Goldberg SN, Kumar G, Wang Y, Gourevitch S, Sosna J, Moon T, Brace CL, Ahmed M. Hepatic thermal ablation: effect of device and heating parameters on local tissue reactions and distant tumor growth. Radiology 2016;281:782–792.
27. Chong J, Wishart DS, Xia J. Using MetaboAnalyst 4.0 for comprehensive and integrative metabolomics data analysis. Curr Protoc Bioinformatics 2019;68:e86.
28. Alfarouk KO, Ahmed SBM, Elliott RL, Benoit A, Alqahtani SS, Ibrahim ME, Bashir AHH, Alhoufie STS, Elhassan GO, Wales CC, Schwartz LH, Ali HS, Ahmed A, Forde PF, Devesa J, Cardone RA, Fais S, Harguindey S, Reshkin SJ. The pentose phosphate pathway dynamics in cancer and its dependency on intracellular pH. Metabolites 2020;10:285.
29. Patra KC, Hay N. The pentose phosphate pathway and cancer. Trends Biochem Sci 2014;39:347–354.
30. Kathagen-Buhmann A, Schulte A, Weller J, Holz M, Herold-Mende C, Glass R, Lamszus K. Glycolysis and the pentose phosphate pathway are differentially associated with the dichotomous regulation of glioblastoma cell migration versus proliferation. Neuro Oncol 2016;18:1219–1229.
31. Kathagen A, Schulte A, Balcke G, Phillips HS, Martens T, Matschke J, Günther HS, Soriano R, Modrusan Z, Sandmann T, Kuhl C, Tissier A, Holz M, Krawinkel LA, Glatzel M, Westphal M, Lamszus K. Hypoxia and oxygenation induce a metabolic switch between pentose phosphate pathway and glycolysis in glioma stem-like cells. Acta Neuropathol 2013;126:763–780.
32. Rozenblum N, Zeira E, Bulvik B, Gourevitch S, Yotvat H, Galun E, Goldberg SN. Radiofrequency ablation: inflammatory changes in the periablative zone can induce global organ effects, including liver regeneration. Radiology 2015;276:416–425.
33. Zhu W, Ye L, Zhang J, Yu P, Wang H, Ye Z, Tian J. PFK15, a small molecule inhibitor of PFKFB3, induces

cell cycle arrest, apoptosis and inhibits invasion in gastric cancer. PLoS One 2016;11:e0163768.
34. Clem BF, O'Neal J, Tapolsky G, Clem AL, Imbert-Fernandez Y, Kerr DA, Klarer AC, Redman R, Miller DM, Trent JO, Telang S, Chesney J. Targeting 6-phosphofructo-2-kinase (PFKFB3) as a therapeutic strategy against cancer. Mol Cancer Ther 2013; 12:1461–1470.
35. Savic LJ, Schobert IT, Peters D, Walsh JJ, Laage-Gaupp FM, Hamm CA, Tritz N, Doemel LA, Lin M, Sinusas A, Schlachter T, Duncan JS, Hyder F, Coman D, Chapiro J. Molecular imaging of extracellular tumor pH to reveal effects of locoregional therapy on liver cancer microenvironment. Clin Cancer Res 2020;26:428–438.
36. Goetze K, Walenta S, Kslazkiewicz M, Kunz-Schughart LA, Mueller-Klieser W. Lactate enhances motility of tumor cells and inhibits monocyte migration and cytokine release. Int J Oncol 2011;39:453–463.
37. Vegran F, Boidot R, Michiels C, Sonveaux P, Feron O. Lactate influx through the endothelial cell monocarboxylate transporter MCT1 supports an NF-B/IL-8 pathway that drives tumor angiogenesis. Cancer Res 2011;71:2550–2560.
38. Frezza C. Metabolism and cancer: the future is now. Br J Cancer 2020;122:133–135.
39. Satriano L, Lewinska M, Rodrigues PM, Banales JM, Andersen JB. Metabolic rearrangements in primary liver cancers: cause and consequences. Nat Rev Gastroenterol Hepatol 2019;16:748–766.
40. Vander Heiden MG, Locasale JW, Swanson KD, Sharfi H, Heffron GJ, Amador-Noguez D, Christofk HR, Wagner G, Rabinowitz JD, Asara JM, Cantley LC. Evidence for an alternative glycolytic pathway in rapidly proliferating cells. Science 2010;329:1492–1499.
41. Calvo MN, Bartrons R, Castaño E, Perales JC, Navarro-Sabaté A, Manzano A. PFKFB3 gene silencing decreases glycolysis, induces cell-cycle delay and inhibits anchorage-independent growth in HeLa cells. FEBS Lett 2006;580:3308–3314.
42. Bando H, Atsumi T, Nishio T, Niwa H, Mishima S, Shimizu C, Yoshioka N, Bucala R, Koike T. Phosphorylation of the 6-phosphofructo-2-kinase/fructose 2,6-bisphosphatase/PFKFB3 family of glycolytic regulators in human cancer. Clin Cancer Res 2005;11:5784–5792.
43. O'Neal J, Clem A, Reynolds L, Dougherty S, Imbert-Fernandez Y, Telang S, Chesney J, Clem BF. Inhibition of 6-phosphofructo-2-kinase (PFKFB3) suppresses glucose metabolism and the growth of HER2+ breast cancer. Breast Cancer Res Treat 2016;160:29–40.
44. Yamamoto T, Takano N, Ishiwata K, Ohmura M, Nagahata Y, Matsuura T, Kamata A, Sakamoto K, Nakanishi T, Kubo A, Hishiki T, Suematsu M. Reduced methylation of PFKFB3 in cancer cells shunts glucose towards the pentose phosphate pathway. Nat Commun 2014;5:3480.
45. Hu S, Balakrishnan A, Bok RA, Anderton B, Larson PE, Nelson SJ, Kurhanewicz J, Vigneron DB, Goga A. 13C-pyruvate imaging reveals alterations in glycolysis that precede c-Myc-induced tumor formation and regression. Cell Metab 2011;14:131–142.
46. Guo Y, Klein R, Omary RA, Yang G-Y, Larson AC. Highly malignant intra-hepatic metastatic hepatocellular carcinoma in rats. Am J Transl Res 2010; 3:114–120.
47. Hill DK, Orton MR, Mariotti E, Boult JKR, Panek R, Jafar M, Parkes HG, Jamin Y, Miniotis MF, Al-Saffar NMS, Beloueche-Babari M, Robinson SP, Leach MO, Chung Y-L, Eykyn TR. Model free approach to kinetic analysis of real-time hyperpolarized 13C magnetic resonance spectroscopy data. PLoS One 2013;8:e71996.
48. Yuan M, Breitkopf SB, Yang X, Asara JM. A positive/negative ion–switching, targeted mass spectrometry–based metabolomics platform for bodily fluids, cells, and fresh and fixed tissue. Nat Protoc 2012; 7:872–881.

Received June 15, 2022. Accepted September 15, 2022.

Correspondence
Address correspondence to: Dr. Leo L. Tsai, BIDMC Department of Radiology, 330 Brookline Avenue, Boston, Massachusetts 02215. e-mail: ltsai1@bidmc.harvard.edu.

CRediT Authorship Contributions

Qianhui Dou (Conceptualization: Supporting; Data curation: Lead; Formal analysis: Lead; Investigation: Lead; Methodology: Lead; Project administration: Lead; Validation: Lead; Visualization: Lead; Writing – original draft: Lead; Writing – review & editing: Supporting)

Aaron K. Grant (Formal analysis: Supporting; Funding acquisition: Supporting; Methodology: Supporting; Software: Lead)

Cody Callahan (Formal analysis: Supporting; Methodology: Supporting; Software: Supporting)

Patricia Coutinho de Souza (Funding acquisition: Supporting; Methodology: Supporting)

David Mwin (Methodology: Supporting)

Adam L. Booth (Formal analysis: Supporting)

Imad Nasser (Formal analysis: Supporting)

Marwan Moussa (Methodology: Supporting; Resources: Supporting)

Muneeb Ahmed (Funding acquisition: Supporting; Methodology: Supporting; Resources: Supporting)

Leo L. Tsai (Conceptualization: Lead; Formal analysis: Supporting; Funding acquisition: Lead; Methodology: Supporting; Project administration: Supporting; Resources: Lead; Software: Supporting; Supervision: Lead; Writing – review & editing: Lead)

Conflicts of interest
The authors disclose no conflicts.

Funding
This work was supported by the Radiological Society of North America (RSNA) RSCH1529 (Leo L. Tsai), the Society of Abdominal Radiology Bosniak (Leo L. Tsai) and Dodds (Patricia Coutinho de Souza and Leo L. Tsai) Awards. In addition, this work was supported in part by the National Institutes of Health through awards R01 CA169470 (Muneeb Ahmed), R01 EB028824, and R01 CA152330 (Aaron K. Grant).